J Nanostruct 14(3): 953-962, Summer 2024

RESEARCH PAPER

Design and Fabrication of TiO_2\G Nanocomposite as Electron Transport Layer for Perovskite QD Solar Cells

Rawaa Abbas Abd Ali *, Majid R. Al-bahrani, Hussein H. Waried

Nanomaterials Laboratory, Department of Physics, College of Science, University of Thi-Qar, Thi-Qar,64001, Iraq

ARTICLE INFO

Article History:
Received 04 April 2024
Accepted 23 June 2024
Published 01 July 2024

Keywords:
CH3NH3PbI3
ETL
HTL
Perovskite
Solar cell

ABSTRACT

This work successfully presented a comparison between two solar cell models based on the development of perovskite layer using quantum dots. The systems (FTO \c-TiO_2-G\ TiO_2-G (ETL)\$CH_3NH_3PbI_3$\$ZrO_2$-G) and (FTO \c-$TiO_2$-G\ TiO_2-G (ETL)\$CH_3NH_3PbI_3$ QD\$ZrO_2$-G) were prepared. The layers that make up the cell were characterized individually after being deposited on FTO glass substrates. X-ray diffraction, FESEM, TEM, FTIR, and Uv-Vis. spectroscopy techniques were utilized to determine the structural, morphological, topological, and optical properties of these layers respectively. XRD pattern of perovskite $CH_3NH_3PbI_3$ showed a polycrystalline structure with (211) as a dominate phase and 78.28 nm as crystallite size. In addition, it had multi-plane prismatic structures with 1.38071±0.78847 µm of the length average and 0.34694±0.18069 µm of the diameter average, and about 72.3 % as a porosity, in the same time, its energy gap reduced from 1.95 eV for $CH_3NH_3PbI_3$ to 1.74 eV for $CH_3NH_3PbI_3$ QD. At the same time, both fill factor and efficiency

How to cite this article
Abd Ali1 R., Al-bahrani M., Waried H. Design and Fabrication of TiO_2\G Nanocomposite as Electron Transport Layer for Perovskite QD Solar Cells. J Nanostruct, 2024; 14(3):953-962. DOI: 10.22052/JNS.2024.03.023

INTRODUCTION

Research in the field of photovoltaic technology has become a priority for researchers in the field of energy [1]. Advanced solar cell research is being carried out in the fields of colloidal quantum dots (CQDs) [2], ink layer[3], dye[4], up conversion[5], and perovskites solar cells[6]. Among these types of solar cells. The crystalline silicon-based solar cells dominate the market share since the 1950s [7]. But the perovskite solar cells have received great interest from scientists due to their cost-effective and high-throughput[8], whereas hybrid perovskite materials have shown great possibilities for solar energy conversion by virtue of their high conversion efficiency, low cost, and The abundance of their preparation materials[9,10]. The perovskite material is an intrinsic (p-type nor n-type) semiconductor [11]. The important obstacle facing perovskite materials for employ in photovoltaic applications is the large and indirect energy gap [12]. Therefore, the general trend has been become focused in many studies on engineering the energy gap to fold this type of solar cell [13]. The general structure of the perovskite is described by the AMX_3 structure, where A is an organic cation, M is a divalent group (cations also) such as (Sn^{2+}, Pb^{2+}), and X is a halide anion (I^-, Br^-, Cl^-) that provides a charge equilibrium for the cations [14], Fig. 1 represents a perovskite crystal structure. There is a high probability of

* *Corresponding Author Email: rawaa.abbas@utq.edu.iq*

exciton generation in perovskite cells within the ETL/perovskite/HTL layered structure by optical injection of charge carriers into both the ETL and HTL layers. Several oxides have been investigated for these layers, including molybdenum trioxide (MoO_3) [11], ZnO [15], Cu_2O NiO [16], SnO_2 [17], and TiO_2 [18]. The interface between the HTL and the perovskite layer is the most important layer for its role in electron collection. TiO_2 got attention due to its appropriate conduction band, easy deposition methods, and chemical stability [19].

MATERIALS AND METHOD

The Spherical TiO_2 nanoparticles (Anatase) (TiO_2, 99.5%, 10-30 nm) and ethanol (99.9%), zirconium (IV) oxide (ZrO_2) (powder, 5 µm, 99%), Methylammonium iodide (CH_3NH_3I), and PbI_2 were obtained from Sigma Aldrich. While, the nanosheets graphene (G, 15 micros) with a platelet morphology were obtained from (skyspring Nanomaterials).

Characterization

The structural properties of the deposited layers were achieved by employment the x-ray diffraction (XRD) spectrum, with Cu Kα1 radiation (λ=1.54060 Å), 30 kV, and 10 mA). Field emission scanning electron microscope (FE-SEM) and transmission electron microscopy TEM (TEM) were used to determine the morphological and topological properties. Moreover, the optical properties were measured based on Uv-Vis. absorbance spectrum (300-800) nm of the wavelength. Perovskite solar cell (PSC) performance was determined based on measurements of the current-density-voltage (I-V) curves.

Fabrication of (FTO \$TiO_2$-G\$CH_3NH_3PbI_3$\$ZrO_2$-G\ Pt)

To obtain the sample of (FTO \c-TiO_2-G\ TiO_2-G (ETL)\$CH_3NH_3PbI_3$\$ZrO_2$-G) and (FTO \c-$TiO_2$-G\ TiO_2-G (ETL)\$CH_3NH_3PbI_3$ QD\$ZrO_2$-G) the same steps must be followed. The compact layer TiO_2\G

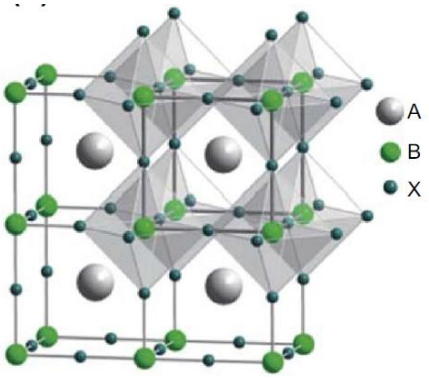

Fig.1. a perovskite crystal structure [11].

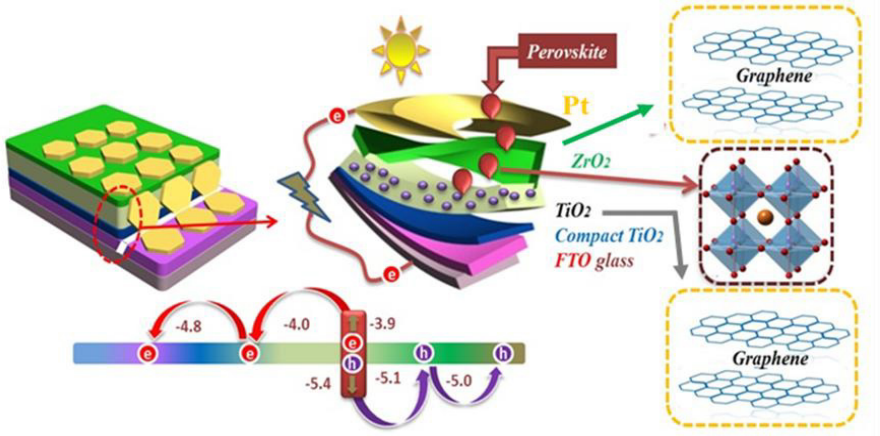

Fig. 2. The structure of the fabricated solar cell.

was deposited by spin coating on pre-transparent conductive glass FTO, and then sintering substrates at 450℃, sintering time is 2h. TiO_2\G film ETL is prepared using the doctor's blade method; by shedding drops of the solution on the FTO\ c-TiO_2\G at room temperature, then left to dry. The fabricated TiO_2\G film (ETL) has been annealed at 450℃ for better adhesion between the film and FTO\c-TiO_2-G Multi-layer. Afterwards, the perovskite $CH_3NH_3PbI_3$ layer was deposited by spin coating on FTO\c-TiO_2-G\$TiO_2$-G ETL. Next, the structural layers were annealed at 100℃. Later, ZrO_2\G layer by spin coating method was deposited and annealed at 100℃. After that, the method of thermal evaporation is used to prepare a grid .Platinum (Pt) wire to be vaporized is placed at a pressure of (10^{-5} tor), and with a surface area of the counter electrode (CE) film (4 cm^2), to fabricated (FTO \$TiO_2$-G\$CH_3NH_3PbI_3$\$ZrO_2$-G\ Pt). In (FTO \c-$TiO_2$-G\ TiO_2-G (ETL)\$CH_3NH_3PbI_3$ QD\$ZrO_2$-G) case, Perovskite layer was prepared according to Zhang et al [20], and replaced by perovskite QD. Fig. 2 presents a structure of the fabricated solar cell.

RESULT AND DISSECTION

Structural properties (XRD analysis)

The XRD analysis of TiO_2/Graphene (ETL) with (Cellulose Ether 0.25) (ETL) showed dominance anatase (nanocrystalline). The dominant phase emerged at 2θ = 25.33° (011), addition to other positions of 2θ= (37.79, 48.04, 62.62, 68.83, 70.22, and 75.154) ° respectively. The possibility of dissociation of titanium dioxide resulting from the presence of both pressure and temperature may lead to hydrogen-bonded to form $H_{0.5}Ti_{0.374}O$ and oxygen to form Ti_3O_5. Meanwhile, no peak appeared related to graphene due to its low percentage of added, except for the shifting in some positions of peaks related to anatase Fig. 3 represents XRD of the prepared deposited ETL film on FTO.

To confirm the structural properties of the raw materials used in the preparation., the X-ray diffraction spectra of both compounds have been compared with (ICDS 00-007-0235 code) for PbI_2 and for CH_3NH_3I according to Stamplecoskie et. al.[14], the dominate phase of PbI_2 was (101) with 86 nm of crystallite size while CH_3NH_3I showed a

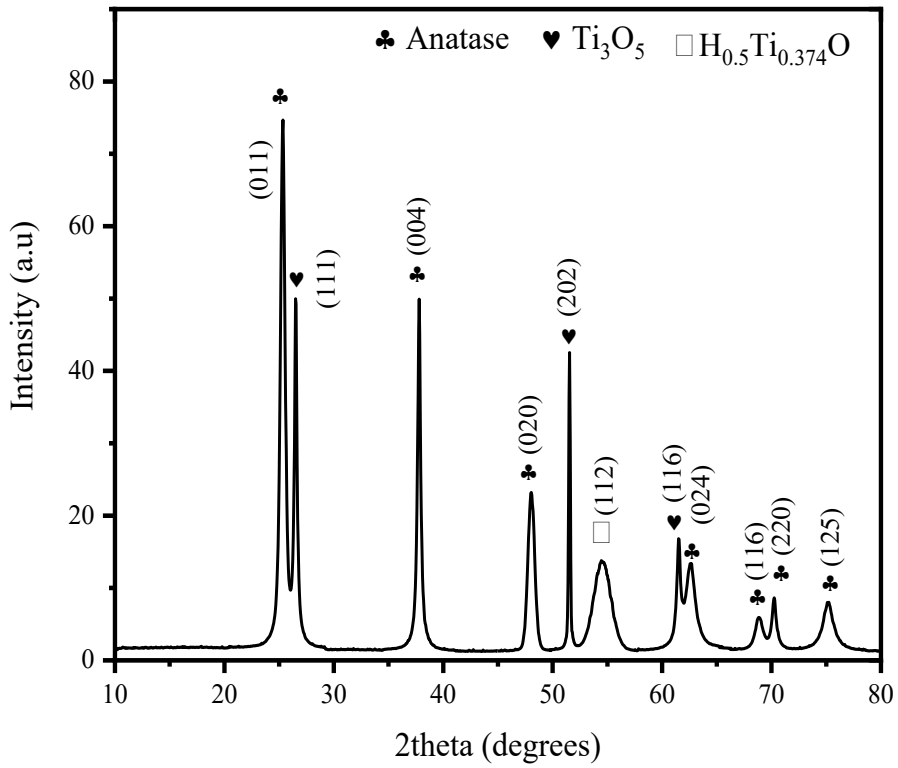

Fig. 3. XRD of the prepared deposited ETL film on FTO.

tetragonal crystalline structure. However, the XRD pattern of $CH_3NH_3PbI_3$ showed a polycrystalline structure with (211) as a dominate phase and 78.28 nm as crystallite size as shown in Fig. 4. That agreement most likely with previous studies [21-23].

TEM and FESEM images

TEM image of $CH_3NH_3PbI_3$ shows a spherical as shape and size distribution between 77 nm to 0.846 µm with about 232 nm of average size as shown in Fig. 5. FESEM image of TiO_2/G film consisted of semi-spherical clusters, were average of 132 nm

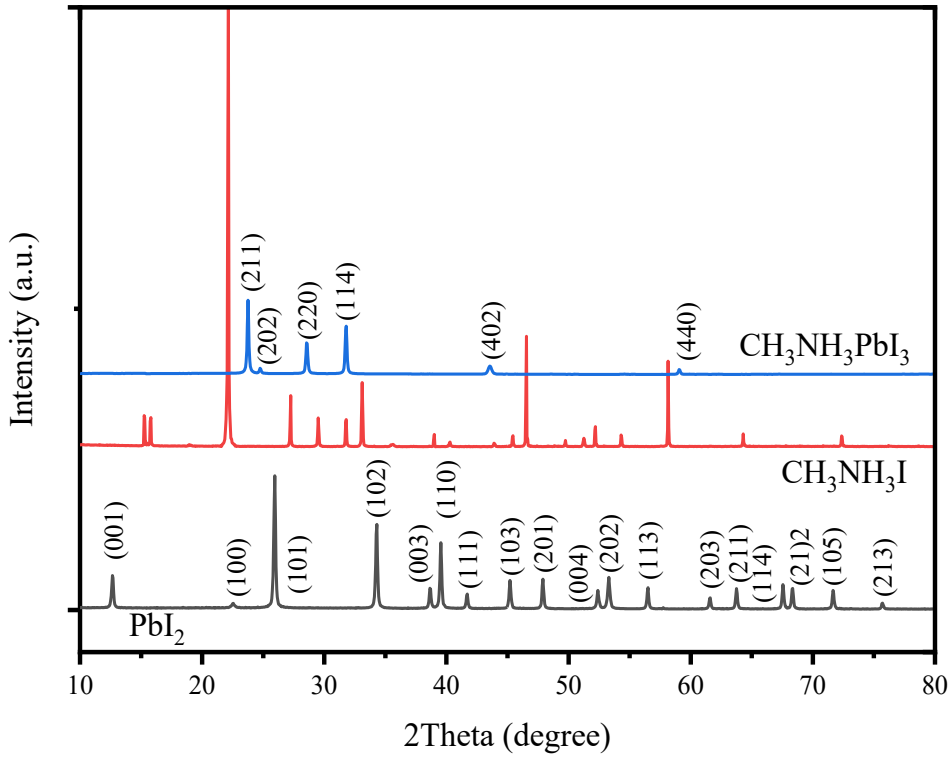

Fig. 4. XRD of the deposited films of PbI2, CH_3NH_3I, and $CH_3NH_3PbI_3$ on FTO

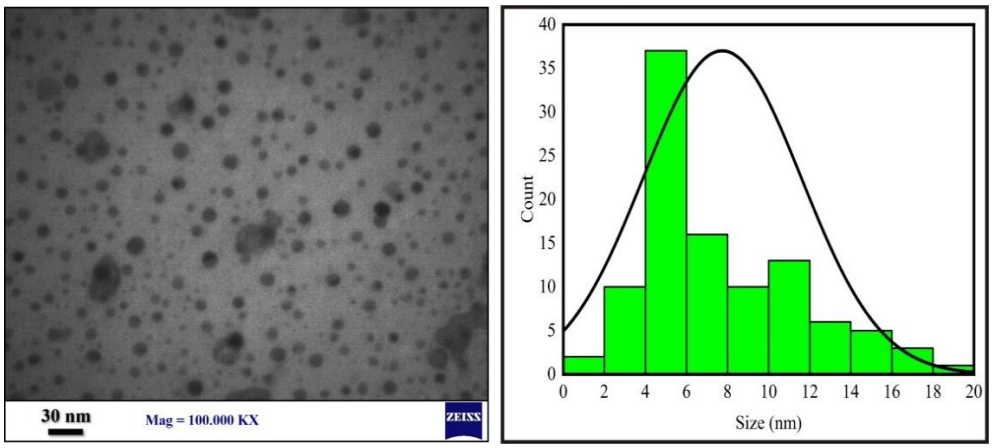

Fig. 5. TEM image and size distribution histogram of $CH_3NH_3PbI_3$ powder

in size. These clusters consist of an aggregate of spherical particles, its size ranges from (7.5 to 46.4) nm with an average of 17.5 nm in size. At the same time, the porosity of this film was about 55% according to Abdullah and Khairurrijal[24] as shown in Fig. 6a. Fig. 6b represent the FESEM image of the used PbI_2 powder. While, the prepared perovskite layer shown as multi-plane prismatic structures with 1.38071±0.78847 µm of the length average and 0.34694±0.18069 µm of the diameter average, and about 72.3 % as a porosity.

Fig. 6 FESEM image and size distribution histogram (a) of deposited TiO_2/G (ETL) film, (b) PbI_2, (c) $CH_3NH_3PbI_3$ film on FTO.

Fourier transform infrared (FTIR)

The dynamic evolution of IR transmission property (Fig. 7) of the prepared perovskite

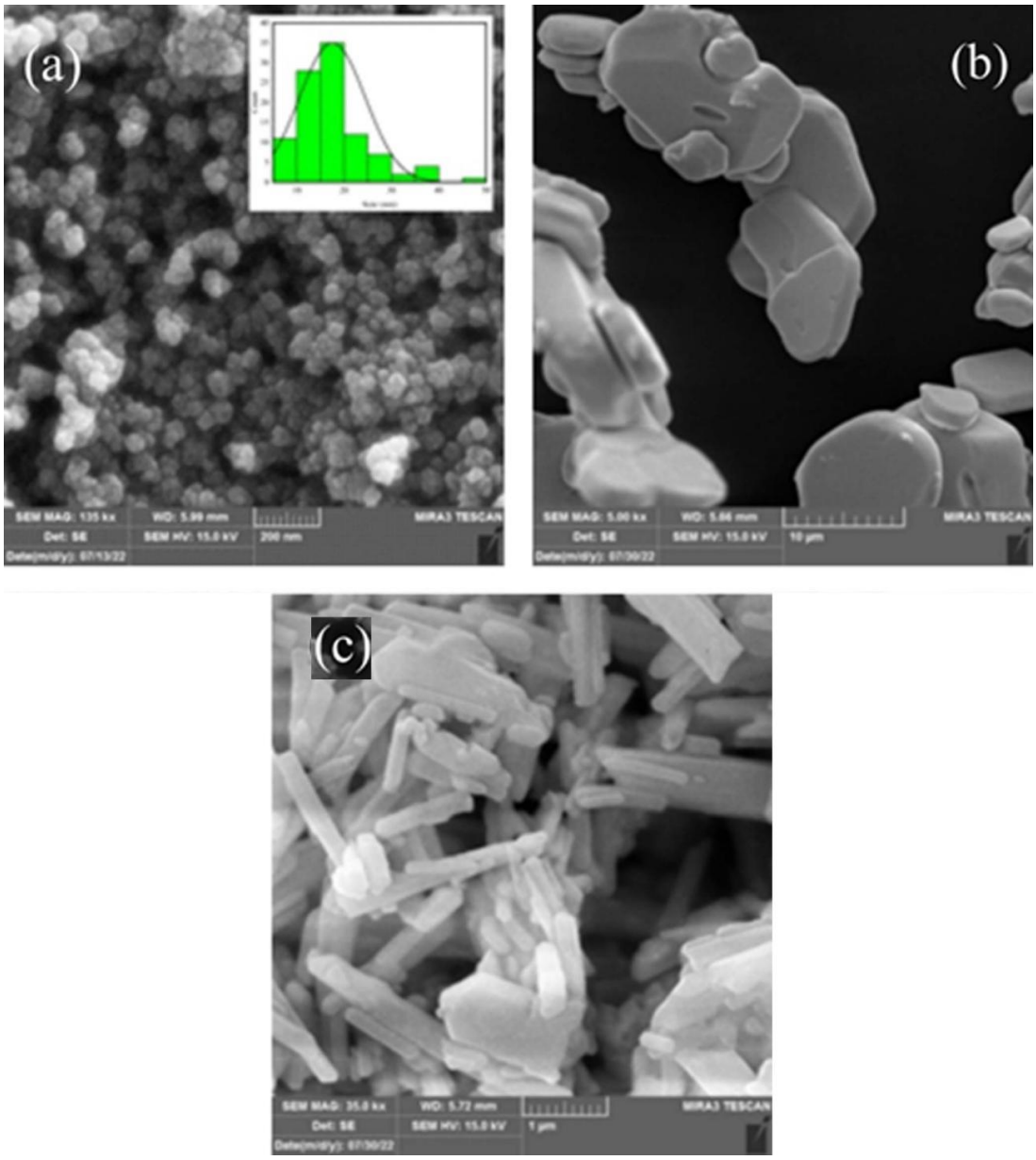

Fig. 6. FESEM image and size distribution histogram (a) of deposited TiO_2/G (ETL) film, (b) PbI_2, (c) $CH_3NH_3PbI_3$ film on FTO.

layer was studied by Fourier transform infrared (FTIR) spectra that were recorded between 400 cm^{-1} to 4000 cm^{-1} of wavenumber as shown in Fig.7. However, the change in the IR spectrum of $CH_3NC_3PbI_3$ and $CH_3NC_3PbI_3$ QD were compared with that of CH_3NC_3I. Generally, It is noticeable that there are changes in both the width and the intensity of the recorded contrast broad peak with all bonds when incorporation the PbI_2. Both peaks (3467 and 3370) cm^{-1} are associated with O-H stretch vibrations in isolated water molecules with hydrogen bonding [25]. The proposed contribution to peaks (3007, 2941, and 1289) cm^{-1} is for C-H bonds. While the peaks of CHO bond were detected at both (2774.3 and 2734) cm^{-1}. All peaks in region 1780 cm^{-1} to 940 cm^{-1} attribute to binding with NH_3^+ and CH_3 bend [26]. It is possible that there is a significant effect of the humidity on the absorbent properties of the material [27]. For the $CH_3NC_3PbI_3$ QD, the peaks suffered a decrease in intensity and shifting in positions with the disappearance of some of them.

Optical Properties

Fig. 8 (a and b) illustrates transmittance of ETL film and ZrO_2-G film on FTO glass for (300-800) nm of wavelength, where it be increase from 69.7% at 350 nm to 90% at 800 nm for ETL. The addition of the thermal treatment (annealing to 450°C), which made to supply complete crystalline which enhanced the electronic transition property, this provides an abundance of transient electrons. Moreover, ZrO_2-G film had about 95% along of the range 300 nm to 800 nm. Energy gap (Eg) was estimated by Tauc equation as follows [28];

$$(\alpha hv)^n = A(hv - Eg) \quad (1)$$

where, A, α, h, v, and Eg are a constant, the absorption coefficient, Plank's and the frequency of incident photon energy respectively, while *n* is (2) with direct energy gab. Based on that, *Eg* of ETL was 2.95 eV, this result is roughly consistent with what has been reported by Shi et al [29].

Fig. 9(a, b) illustrate absorption behavior of PbI_2, CH_3NH_3I, $CH_3NH_3PbI_3$ and $CH_3NH_3PbI_3$ QD. There are a noted deceasing in the transmittance of $CH_3NH_3PbI_3$ in the region (346-622) nm compared both PbI_2 and CH_3NH_3I. On the other side, due

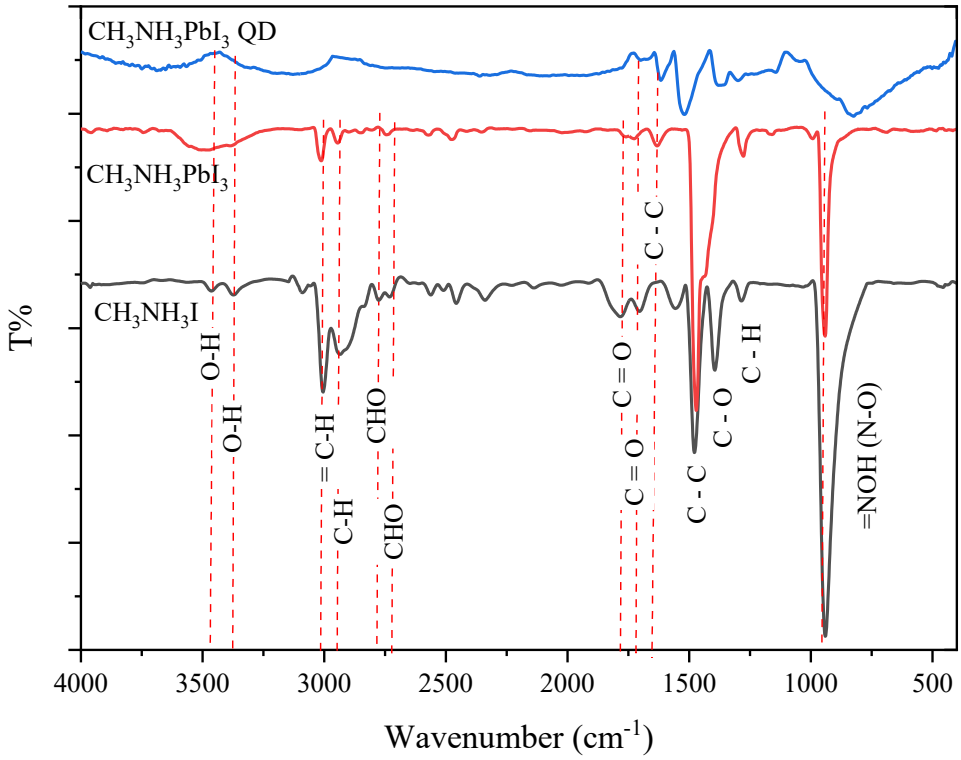

Fig. 7. FTIR spectrum of both CH_3NH_3I and $CH_3NH_3PbI_3$

to the greater absorption coefficients of all PbI_2, CH_3NH_3I, and $CH_3NH_3PbI_3$ (>$10^4 cm^{-1}$), indicates the presence of a direct energy gap transition. E_g decreased from 2.03 eV and 2.08 eV for PbI_2 and CH_3NH_3I, respectively to 1.95 eV for $CH_3NH_3PbI_3$ as illustrated in Fig. 10. The formation of a tetragonal perovskite phase with the reaction of lead halides with CH_3NH_3I may be a lead change in the optical bandgap. The low difference in the bandgap value can be indicative of the partial retention of iodine ions without bonding [30].While the absorbance of $CH_3NH_3PbI_3$ was 88.7% at 550 nm of the wave length. Moreover, $CH_3NH_3PbI_3$ QD film had a linear increasing of absorbance along (300-800) nm of wavelength from 82.5 to 94.5 respectively as shown in Fig. 9(c and d).

Characterization of solar cell

To estimate the quality of a solar cell and its electrical behavior; current-voltage (I-V) measurements were achieved. I-V characteristics of the prepared (FTO\$TiO_2$-G\$CH_3NH_3PbI_3$\$ZrO_2$-G\Pt) and (FTO \$TiO_2$-G\$CH_3NH_3PbI_3$ QD\$ZrO_2$-G\Pt) solar cells under 100 $mW.cm^{-2}$ of the illumination powers with the forward applied voltage is illustrated in Fig. 10. The dark voltage (V_{oc}), short circuit current (I_{sc}), and fill factor (FF) parameters were determined from I-V curves of the solar cell. Fill factor can be calculate by the following [31].

$$FF = \frac{V_{mp} I_{mp}}{V_{oc} I_{sc}} \quad (2)$$

Where V_{mp} is the voltage at the maximum power point; I_{mp} is the current at the maximum power, P; V_{os} is the no-load voltage; I_{sc} is the short-circuit current. While the efficiency, PCE can be calculate by the following [21],

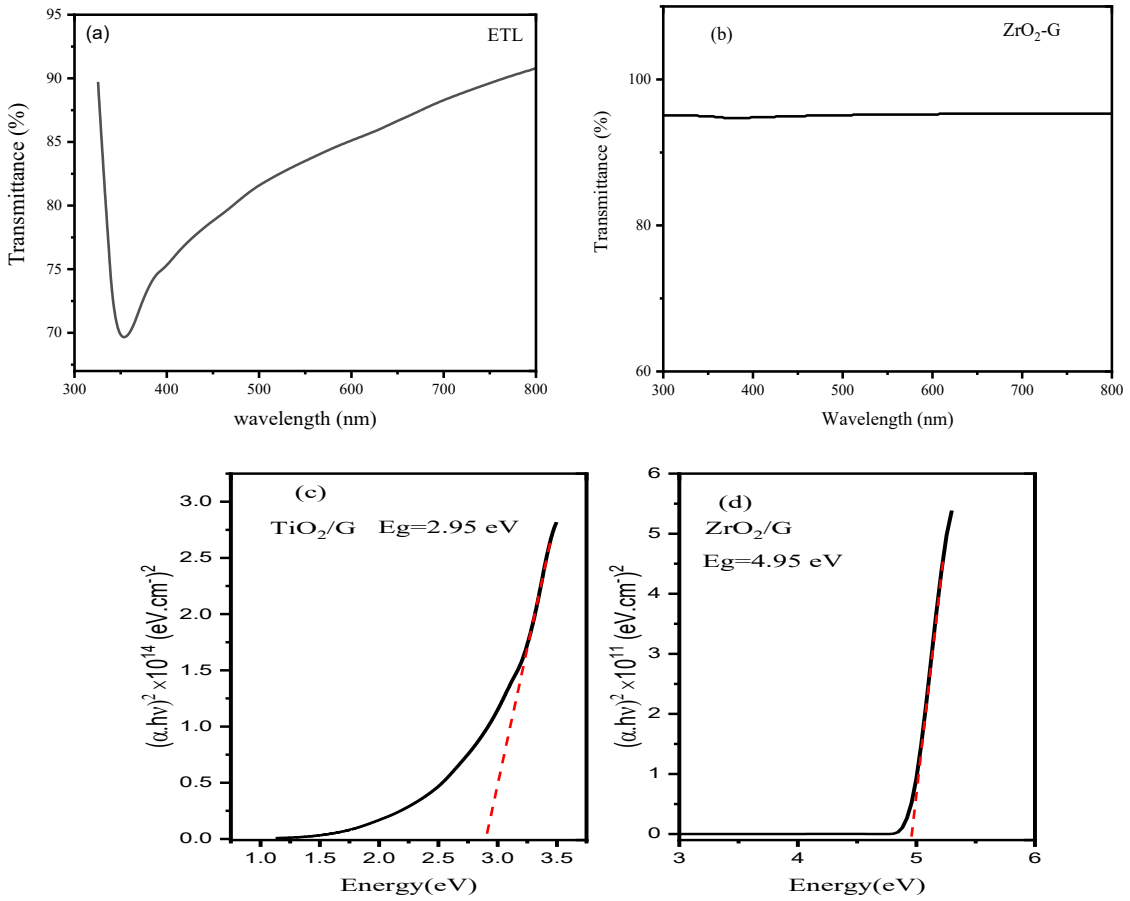

Fig. 8. the transmittance of (a) TiO_2\G (ETL) and (b) ZrO_2\G (HTL), the energy gap of (c) TiO_2\G (ETL), and (d) ZrO_2/G (HTL) films on FTO.

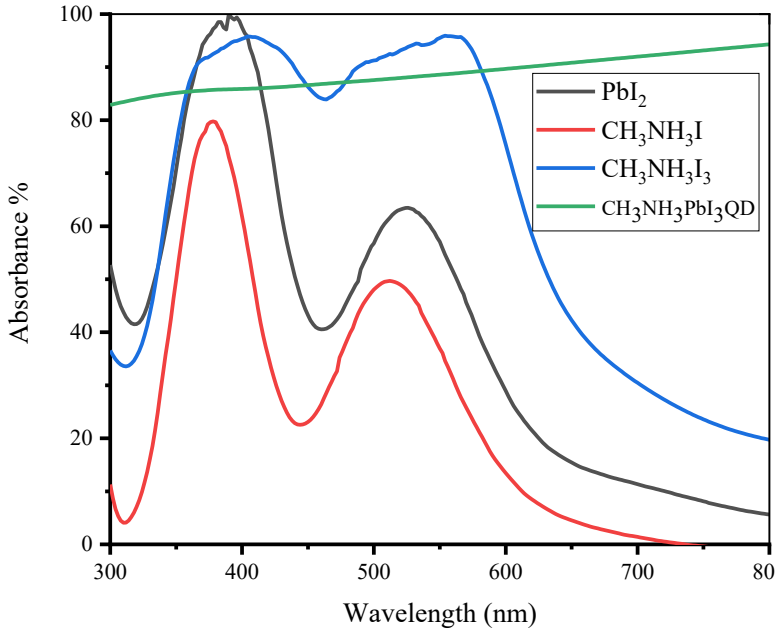

Fig. 9. absorption behavior of PbI_2, CH_3NH_3I, $CH_3NH_3I_3$, and CH_3NH_3PbIQD.

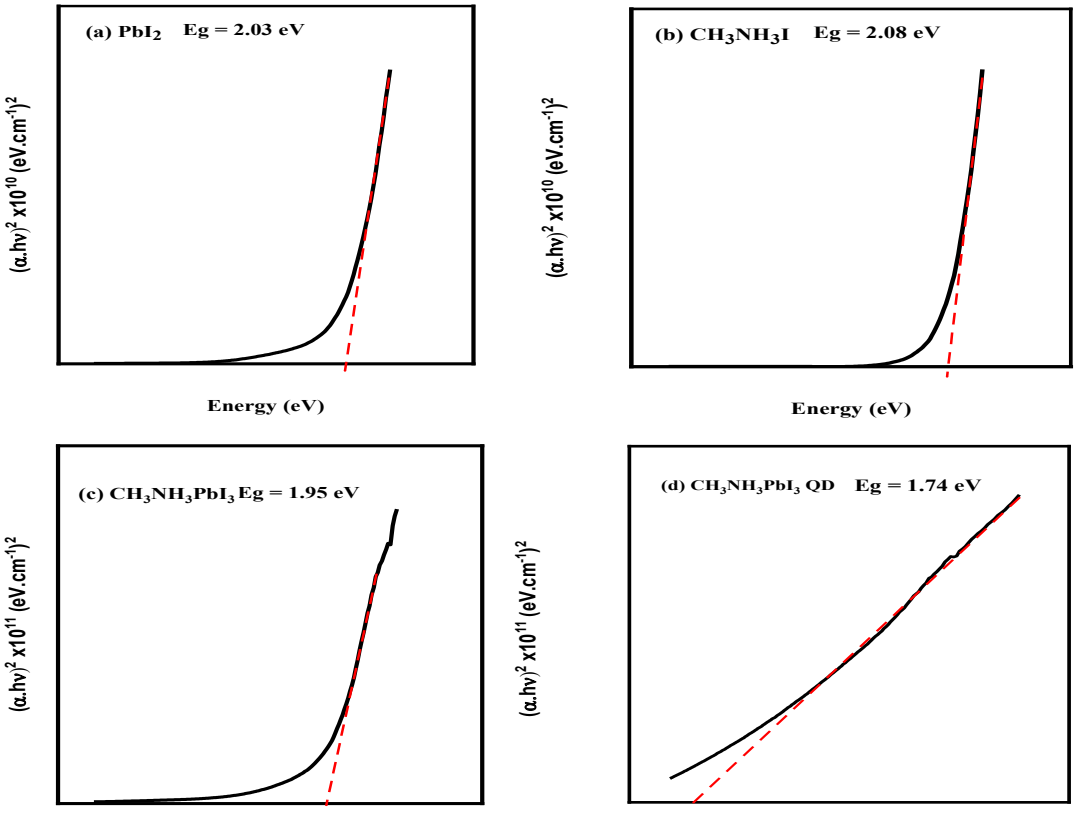

Fig. 10. the variation of energy gap for (a) PbI_2,(b) $CH_3NH_3I_3$,(c) $CH_3NH_3PbI_3$, and (d) $CH_3NH_3PbI_3QD$.

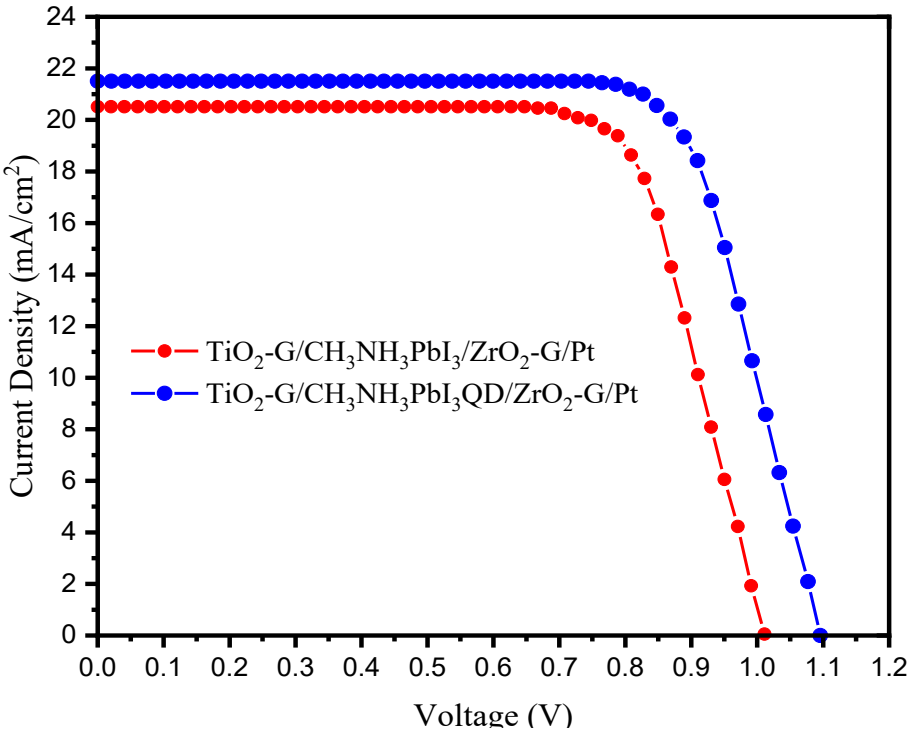

Fig. 11. current-voltage characteristic of the prepared solar cells

Table 1. The prepared solar cell.

Prepared solar cell	V_{oc} (V)	J_{sc} (mA/cm²)	FF	η%
FTO \$TiO_2$-G\$CH_3NH_3PbI_3$\$ZrO_2$-G\Pt	1.04	20.40	0.72	15.487
FTO \$TiO_2$-G\$CH_3NH_3PbI_3$ QD\$ZrO_2$-G\Pt	1.10	21.13	0.73	16.967

$$\eta = \frac{FF \times V_{oc} \times I_{sc}}{P_{in}} \quad (3)$$

Where P_{in} is the incident light power. If the conduction band edge of the quantum dots is located between the conduction edge of the perovskite and the top occupied molecular orbital of the carriers transition layer, the transition of charge carriers is improved, thus improving the value of the fill factor, which leads to the improvement of the conversion efficiency of the solar cell [32].

The prepared solar cells have 15.48% and 16.96% as an efficiency for both FTO \$TiO_2$-\$CH_3NH_3PbI_3$\$ZrO_2$-G\Pt and FTO \$TiO_2$-G\$CH_3NH_3PbI_3$ QD\$ZrO_2$-G\Pt respectively as shown in Fig. 11 and Table 1.

CONCLUSION

This study succeeded in presenting a perovskite solar cell based on perovskite QD material. Because ZrO_2 and TiO_2/G possess energies gap in the deep UV and Visible regions respectively, they generate an abundance of electron-hole pairs that improves the transition of holes to graphene and electron traps in ZrO_2. Moreover, the presence of the interface between HTL and the perovskite layer and the interface between ETL and the perovskite layer provides a suitable position for the conduction band edge of the quantum dots in relation to the perovskite conduction edge and the occupied molecular orbital of the HTL and ETL. That improved the factor of the fill factor. Therefore، leads to the improvement of the

conversion efficiency of the solar cell. So was the case with the carriers in ETL.

CONFLICT OF INTEREST

The authors declare that there is no conflict of interests regarding the publication of this manuscript.

REFERENCES

1. Al-Kayiem HH, Mohammad ST. Potential of Renewable Energy Resources with an Emphasis on Solar Power in Iraq: An Outlook. Resources. 2019;8(1):42.
2. Zheng S, Chen J, Johansson EMJ, Zhang X. PbS Colloidal Quantum Dot Inks for Infrared Solar Cells. iScience. 2020;23(11):101753-101753.
3. Engberg S, Martinho F, Gansukh M, Protti A, Küngas R, Stamate E, et al. Spin-coated [Formula: see text] solar cells: A study on the transformation from ink to film. Sci Rep. 2020;10(1):20749-20749.
4. Rehman AU, Ullah N, Saeed MA, Khalil UK. Enhanced Absorption Performance of Dye-Sensitized Solar Cell with Composite Materials and Bilayer Structure of Nanorods and Nanospheres. Metals. 2022;12(5):852.
5. Ghazy A, Safdar M, Lastusaari M, Savin H, Karppinen M. Advances in upconversion enhanced solar cell performance. Sol Energy Mater Sol Cells. 2021;230:111234.
6. Olaleru SA, Kirui JK, Wamwangi D, Roro KT, Mwakikunga B. Perovskite solar cells: The new epoch in photovoltaics. Solar Energy. 2020;196:295-309.
7. Glunz SW, Preu R. Crystalline Silicon Solar Cells – State-of-the-Art and Future Developments. Comprehensive Renewable Energy: Elsevier; 2022. p. 293-324.
8. Osman B, Abdolkader T, Ahmed I. A Review of Perovskite Solar Cells. International Journal of Materials Technology and Innovation. 2021;0(0):0-0.
9. Manser JS, Saidaminov MI, Christians JA, Bakr OM, Kamat PV. Making and Breaking of Lead Halide Perovskites. Acc Chem Res. 2016;49(2):330-338.
10. Song Z, Watthage SC, Phillips AB, Heben MJ. Pathways toward high-performance perovskite solar cells: review of recent advances in organo-metal halide perovskites for photovoltaic applications. Journal of Photonics for Energy. 2016;6(2):022001.
11. Lim EL, Yap CC, Jumali MHH, Teridi MAM, Teh CH. A Mini Review: Can Graphene Be a Novel Material for Perovskite Solar Cell Applications? Nano-micro letters. 2018;10(2):27-27.
12. Hu Z, Lin Z, Su J, Zhang J, Chang J, Hao Y. A Review on Energy Band-Gap Engineering for Perovskite Photovoltaics. Solar RRL. 2019;3(12).
13. Bush KA, Frohna K, Prasanna R, Beal RE, Leijtens T, Swifter SA, et al. Compositional Engineering for Efficient Wide Band Gap Perovskites with Improved Stability to Photoinduced Phase Segregation. ACS Energy Letters. 2018;3(2):428-435.
14. Stamplecoskie KG, Manser JS, Kamat PV. Dual nature of the excited state in organic–inorganic lead halide perovskites. Energy & Environmental Science. 2015;8(1):208-215.
15. Dadashbeik M, Fathi D, Eskandari M. Design and simulation of perovskite solar cells based on graphene and TiO2/graphene nanocomposite as electron transport layer. Solar Energy. 2020;207:917-924.
16. Lekesi LP, Koao LF, Motloung SV, Motaung TE, Malevu T. Developments on Perovskite Solar Cells (PSCs): A Critical Review. Applied Sciences. 2022;12(2):672.
17. Chen P, Bai Y, Wang S, Lyu M, Yun JH, Wang L. Perovskite Solar Cells: In Situ Growth of 2D Perovskite Capping Layer for Stable and Efficient Perovskite Solar Cells (Adv. Funct. Mater. 17/2018). Adv Funct Mater. 2018;28(17).
18. Gaur D, Sharma S, Ghoshal SK. Modified structures, optical and photovoltaic characteristics of low energy ions beam irradiated TiO2/TiO2-Graphene thin films as electron transport layer in perovskite solar cell. Materials Today: Proceedings. 2021;43:3826-3832.
19. Wang Y, Wan J, Ding J, Hu JS, Wang D. A Rutile TiO_2 Electron Transport Layer for the Enhancement of Charge Collection for Efficient Perovskite Solar Cells. Angew Chem Int Ed. 2019;58(28):9414-9418.
20. Colloidal Synthesis of Air-Stable $CH_3NH_3PbI_3$ Quantum Dots by Gaining Chemical Insight into the Solvent Effects. American Chemical Society (ACS).
21. Zdyb A. Perovskite Solar Cells. Third Generation Solar Cells: Routledge; 2022. p. 69-101.
22. Awino C, Odari V, Dittrich T, Prajongtat P, Sakwa T, Rech B. Investigation of Structural and Electronic Properties of $CH_3NH_3PbI_3$ Stabilized by Varying Concentrations of Poly(Methyl Methacrylate) (PMMA). Coatings. 2017;7(8):115.
23. Manukyan KV, Yeghishyan AV, Moskovskikh DO, Kapaldo J, Mintairov A, Mukasyan AS. Mechanochemical synthesis of methylammonium lead iodide perovskite. Journal of Materials Science. 2016;51(19):9123-9130.
24. Abdullah M, Khairurrijal K. A Simple Method for Determining Surface Porosity Based on SEM Images Using OriginPro Software. Indonesian Journal of Physics. 2016;20(2):37-40.
25. Idígoras J, Todinova A, Sánchez-Valencia JR, Barranco A, Borrás A, Anta JA. The interaction between hybrid organic–inorganic halide perovskite and selective contacts in perovskite solar cells: an infrared spectroscopy study. Physical Chemistry Chemical Physics. 2016;18(19):13583-13590.
26. Patel JB, Milot RL, Wright AD, Herz LM, Johnston MB. Formation Dynamics of $CH_3NH_3PbI_3$ Perovskite Following Two-Step Layer Deposition. The Journal of Physical Chemistry Letters. 2015;7(1):96-102.
27. Haque MA, Syed A, Akhtar FH, Shevate R, Singh S, Peinemann K-V, et al. Giant Humidity Effect on Hybrid Halide Perovskite Microstripes: Reversibility and Sensing Mechanism. ACS Applied Materials & Interfaces. 2019;11(33):29821-29829.
28. Yaseen MT. Preparation and Characterization of Silicon Carbide by Pulse Laser Deposition as Heterojunction Solar Cell. Neuroquantology. 2020;18(2):50-55.
29. Shi X, Liu X, Zeng H. ZrO_2 quantum dots/graphene phototransistors for deep UV detection. Materials Research Bulletin. 2017;96:458-462.
30. Heydari Z, Abdy H, Ghaziani MP, Kolahdouz M, Asl-Soleimani E, Masnadi-Shirazi M. Effect of CH3NH3I/CH3NH3Br precursors on the structural and surface morphology properties of the electrodeposited methylammonium lead–mixed halide perovskite films. J Solid State Electrochem. 2020;25(2):583-590.
31. Kanareykin AI. On the correctness of calculating the Fill Factor of the solar module. IOP Conference Series: Earth and Environmental Science. 2021;808(1):012018.
32. Cha M, Da P, Wang J, Wang W, Chen Z, Xiu F, et al. Enhancing Perovskite Solar Cell Performance by Interface Engineering Using $CH_3NH_3PbBr_{0.9}I_{2.1}$ Quantum Dots. Journal of the American Chemical Society. 2016;138(27):8581-8587.